SSC19-WKII-07

Design and On-Orbit Experience of Reaction Wheels for Small Satellites

Walter Frese, Udo Renner, Klaus Brieß, Zizung Yoon
Department of Aeronautics and Astronautics, Technische Universität Berlin
Marchstr. 12, 10587 Berlin, Germany; +49 30 314 25611
walter.frese@tu-berlin.de

ABSTRACT

The history of reaction wheel development at the Technische Universität Berlin (TUB) begins early in the 90s. Since then many of these reaction wheels performed on-orbit without a single failure as a part of six micro- and nanosatellite missions. The last one is the *S band Network for co-operating Satellites* (S-Net). S-Net is a cluster of four nanosats successfully launched in February 2018. Since then a number of communication experiments using intersatellite links have been performed by the S-Net satellites. This paper is focusing on the design and on the on-orbit performance of the reaction wheels for S-Net nanosatellites. The design is based on COTS and differs considerably from the state-of-the-art one. The wheel is pressurized, allowing higher rotation speeds due to a better thermal performance as well as the use of commercial motors without any changes in ball bearings and their lubrication. Due to a better ball bearing friction the performance and, consequently, the failure tolerance have increased significantly. The wheels can run at higher speeds continuously allowing their use within momentum bias platforms. A novel suspension system helped to optimize the misalignment of the rotational axis compared to a simple spiral spring based suspension used for TUB wheels earlier. A further outstanding feature is the implementation of some additional control loops alongside with the standard current, speed and torque control. The use of built-in internal angular velocity sensors makes satellite velocity and satellite angle control modes possible. For some operational scenarios, especially for such with high agility requirements, it can be advantageous because these control loops can be closed with a higher frequency as if would be possible with a centralized external attitude controller. The system is characterized by a low steady-state power consumption of 220 mW at the zero motor speed and under 1.5 W at the maximum speed, has the dimensions of 65 x 65 x 55 mm^3 and a weight of less than 320 g. Two wheel modifications for different satellite classes with slightly different rotor geometry exist. The angular momentum can be as high as 45 mNms. The modular design allows a scale-up without significant changes in mechanics and electronics. Finally, future work based on the described design is discussed.

INTRODUCTION

Reaction wheels are currently being used in various missions with small satellites that require high-accuracy pointing capabilities. First reaction wheels from Technische Universität Berlin (TUB) have been developed for microsatellites and verified on-orbit for the first time on TUBSAT-N in 1998 [1]. Since then, many of them have been used in attitude control systems (ACS) of TUBSAT satellites without a failure [2], [3]. Later, in 2006 the first CubeSat from TUB – BEESAT-1 – has been successfully launched [4]. BEESAT-1 marks a new level of miniaturization of the satellites from TUB. A need for smaller reaction wheels emerged and led to a new development. This paper is focused on the design and on the on-orbit results of newly developed reaction wheels for nanosatellites. The flight results are gathered during two satellite missions – TechnoSat and S-Net (2017 and 2018 respectively). The emphasis has been laid on the S-Net mission.

The primary mission goal of S-Net is to demonstrate an S band based multipoint ISL network within a nanosatellite constellation. The goal can be subdivided into following objectives: i) demonstration of multipoint ISL with S band transceiver, ii) verification of ISL communication protocols, iii) precise analysis of nanosatellite formation behavior considering orbital perturbations and, finally, iv) demonstration of the practical feasibility of nanosatellites for communication applications.

The four S-Net nanosatellites – with a mass of 8.7 kg each – were successfully launched in 2018 into a Sun-synchronous low Earth orbit. The satellites were designed for a lifetime of one year; the satellite bus is fault-tolerant with only few single points of failure (SPOF). The network communication is maintained by a set of predefined rules operating independently of all four satellites.

SYSTEM OVERVIEW

The reaction wheel (see Figure 1) is a single unit with dimensions of 65 x 65 x 55 mm^3 and a weight of less than 320 g (two configurations exist with slightly

different flywheel's moments of inertia). Table 1 gives an overview over the specifications of the reaction wheels.

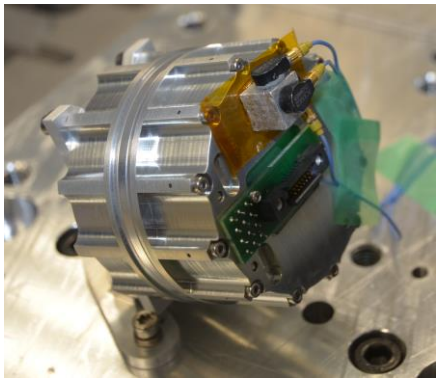

Figure 1: Reaction Wheel in Test Environment.

The wheel has two mechanical interfaces for flexible integration and one power and data interface unified in a single connector. Up to five different control modes can be selected, e.g. traditional ones like the motor rate mode and the torque mode or (due to an integrated gyroscope) some special modes like the satellite angular velocity mode.

Table 1: Specifications

Parameter	Value	Unit
Mass (depending on configuration)	280…320	g
Dimensions	65 x 65 x 55	mm^3
Radiation tolerance	10	krad (Si)
Vibration	20	g RMS
Shock	1500	g
Operation temperature range	-20…+50	°C
Angular momentum (6000 rpm)	up to 45	mNm s
Max. rotation speed (steady state)	6000	rpm
Nominal torque (ramp mode)	0.1	mNm
Maximal torque	1.9	mNm
Moment of inertia (rot. mass)	up to 730	gcm^2
Nominal voltage (1)	12	V
Standby power	220	mW
Power at max. rotation speed	1.35	W
Max. power (2)	< 20	W
Data interface	UART, CAN	
(1) unregulated (2) can be limited by the software		

Figure 2 depicts an explosion view of the reaction wheel. A flywheel (item No. 6) is attached to the shaft of a brushless DC electric (BLDC) motor (item No. 2). A newly developed suspension system is used to reduce dynamic loads to the bearings of the motor during launch (e.g. items No. 1, 3, 5, 10, 22). The aforementioned components as well as the both printed circuit boards (PCB) belonging to the wheel drive electronics (items No. 11 and 12) are integrated into both main structural components (items No. 7 and 8). The flywheel is made of brass; most of other components are manufactured from an Aluminum alloy. The structure is hermetically sealed to protect the ball bearings of the motor against vaporization of the lubricants and for an improved thermal performance. The electric signals are guided through the structure with twelve single vacuum feedthroughs (item No. 13). The sealing is realized with two-component adhesives.

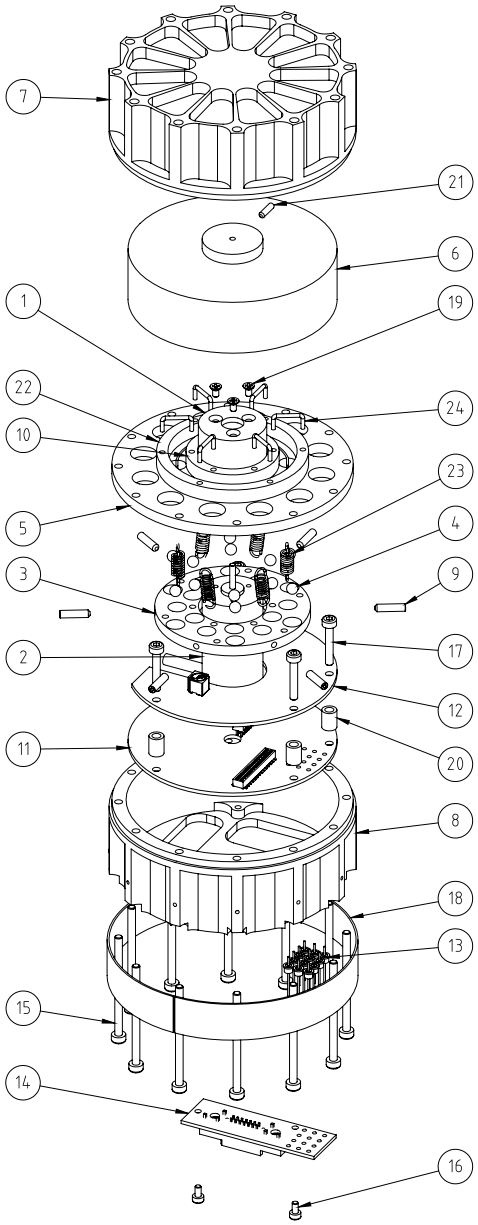

Figure 2: Explosion View.

ELECTROMECHANICS

Overview

The main component is a commercial off-the-shelf (COTS) brushless DC motor (BLDC) with three Hall-effect sensors and a life-time lubrication. The shaft bearings are preloaded ball bearings. The bearings and the lubricant are optimized for long-life and low-friction in terrestrial environment. For shortening of procurement times and to reduce the costs it might be very helpful to avoid any customizations of commercial components. One of the main difficulties with such a motor is the lubricant that is not suitable for operation in vacuum by default and would easily vaporize. To make the motor suitable for space applications as it is and without any modifications all reaction wheels of the TUB have been sealed since the first designs from the 90s. This approach has paid off. The other difficulty is connected to the small dimensioned ball bearings for the shaft that are not able to withstand the high dynamic loads during launch because of a relatively high mass of the flywheel on the motor's shaft. To solve this problem a novel suspension system for the motor and for the flywheel was developed. It offers a low axial misalignment and is easy to manufacture. The flywheel is balanced on ground in-system, firmly attached to the shaft of the motor.

Suspension System

Figure 3 depicts the main parts of the suspension system. The purpose of the system is to reduce the level of dynamic loads going through the ball bearings of the motor during launch. The motor is integrated into a free-hanging frame. A flat disc called bracket is firmly attached to wheel's casing components. The flexible connection between bracket and motor's frame is carried out through a component called bridge. A precise alignment of frame, bracket and bridge in nominal (unloaded) configuration is realized with help of steel balls clamped between these components. The parts of the suspension system are held together with spiral springs (see Figure 4). The springs are dimensioned to keep the parts of suspension system in contact on ground; the combined spring force is slightly higher than the weight of the motor and flywheel together. In presence of high loads (during launch) the springs will allow a tilting of the frame primary in two axes. Also both translations along the rotational axis are possible. The casing is designed so that the form its inner surface reproduces the shape of the flywheel with a small gap of 0.5 millimeters. The aforementioned tilting of the rotational axis or the translator movements of the motor and attached flywheel will lead to hammering of the flywheel into casing. The dynamic loads are 'shortened' on a direct way from the most massive component (flywheel) to the structure of the wheel and later to the structure of the satellite. These loads are prevented from going all the way through the shaft, the bearings and the motor.

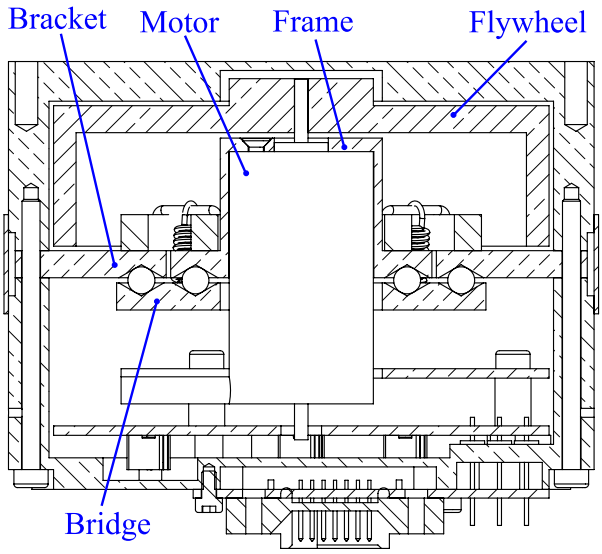

Figure 3: Main Elements of Motor's Suspension System.

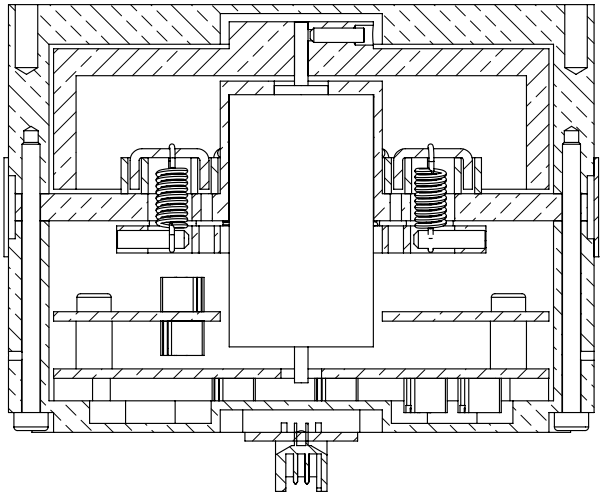

Figure 4: Section through Spiral Springs.

WHEEL DRIVE ELECTRONICS

Overview

Wheel drive electronics (WDE) with a digital interface (differential signal UART or CAN) offers following standard control loops in one axis in a single solution: current control, speed control and torque control. Using of an integrated MEMS gyroscope makes two further control loops possible: satellite angular velocity control and satellite angle control. A barometric pressure sensor is integrated into the sealed volume of the wheel.

Measurements provided by the sensors are offered on the digital interface together with values for voltages, currents, temperatures and some control parameters like motor speed, torque and satellite angular velocities.

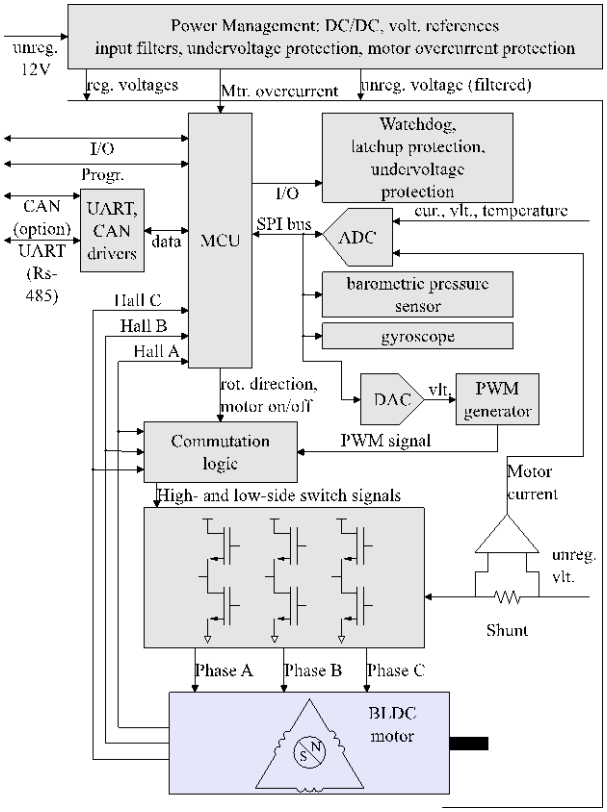

Figure 5: Simplified Block Diagram of Wheel Drive Electronics.

The current through the coils of the brushless motor is controlled with high-side and low-side MOSFET switches in H-bridge configuration. The pulse-width modulated (PWM) waveform is used to control the current through the coils. A 120° commutation based on Hall-effect sensors is implemented. The control loops are implemented in software of a microcontroller unit (MCU). An ultra-low power microcontroller is used. The design of the WDE is optimized for power saving. The standby power consumption (MCU is always at the highest load) is approximately 220 mW.

Pulse Width Modulation

To control the electric current through the coils of the BLDC motor a PWM signal with a wide range of duty cycles needs to be generated. The simplest method is to do that directly in the microcontroller, which requires a timer, six output pins (one for each of the high-side and low-side switches) and a clock rate high enough to generate a signal of at least 10 kHz with a precision of at least 12 bit. The microprocessor clock rate and the energy consumption can be kept low if the PWM generation would occur externally. It can be done using an integrated solution based on a single voltage-controlled IC with a very small footprint. Here a different solution is proposed. It is based on a well-known discrete circuit build up with operational amplifiers and voltage comparators. One of the advantages: the circuit can be re-designed using Hi-Rel or Rad-Hard components.

Figure 6 shows the realized circuit. It utilizes a triangle wave generator and comparator to generate a PWM signal with a duty cycle that is inversely proportional to the input voltage. It works with a single 3.3 V power supply and generates a PWM waveform with a frequency f_{TRI} of approximately 15 kHz and requires a single reference voltage V_{REF} of 2.048 V. V_{REF1} is generated from V_{REF} through a voltage divider and should be approximately a half of the supply voltage (3.3 V). Other frequencies can be easily realized by change of passive components using following equation:

$$f_{TRI} = \frac{R_6}{4R_7R_5C_3} \qquad (1)$$

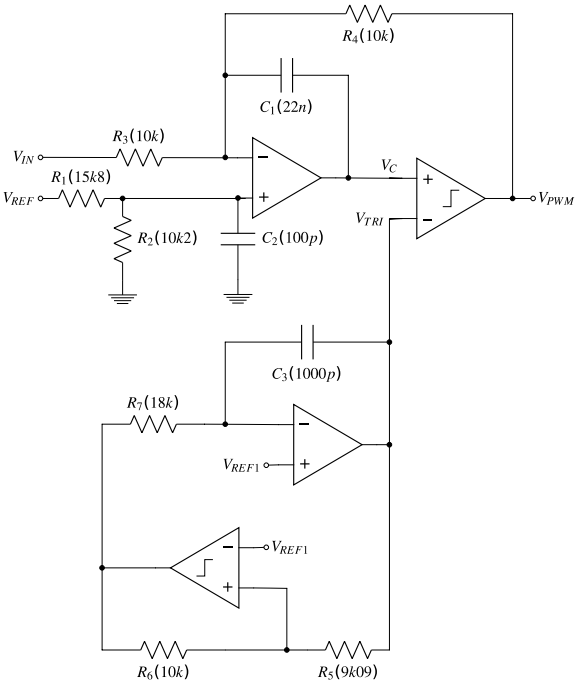

Figure 6: Pulse Width Generator Circuit.

Figure 7 shows a step response of the circuit. The input (control) voltage V_{IN} is generated by a 16-bit digital-

to-analog converter (DAC) and used to set the duty cycle of the PWM output. The PWM waveform is generated by the output comparator that works with V_{TRI} and V_C inputs. Figure 7 depicts the two inputs to the comparator (middle) as well as the resulting output (bottom). The bandwidth of the system is limited by C1 in order to ensure the stability of the system. It is why the system needs some time to change the duty cycle after a step of V_{IN}.

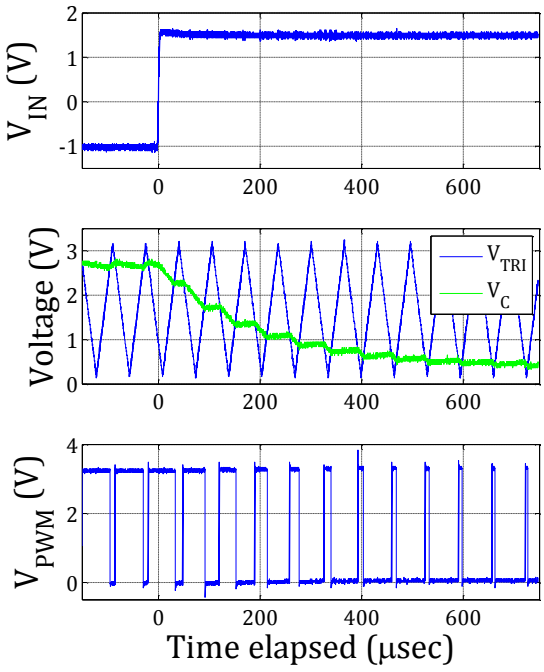

Figure 7: Step Response of Pulse Width Generator.

The footprint for the solution based on MSOP packages measures 16 x 25 mm^2 (see Figure 8, one side PCB layout). Dual operational amplifier and comparator ICs are used to save PCB space.

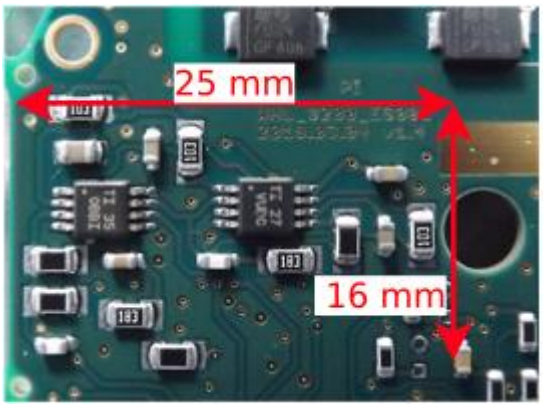

Figure 8: Footprint of PWM Circuit.

Commutation

There are two commutation techniques for brushless motors equipped with Hall-effect sensors: trapezoidal and sinusoidal control. Assumed, the torque ripple at low speeds is not critical, the less complex trapezoidal method would probably be a better choice. The sensor signals (H_A, H_B, H_C) can be converted to the low side ($Q_{A-L}, Q_{B-L}, Q_{C-L}$) and high side ($Q_{A-H}, Q_{B-H}, Q_{C-H}$) drive signals using following Boolean expressions:

$$Q_{A-H} = \overline{H}_A H_B,\ Q_{B-H} = \overline{H}_B H_C,\ Q_{C-H} = \overline{H}_C H_A \quad (2)$$

$$Q_{A-L} = H_A \overline{H}_B,\ Q_{B-L} = H_B \overline{H}_C,\ Q_{C-L} = H_C \overline{H}_A \quad (3)$$

And the equations for the other rotational direction:

$$Q_{A-L} = \overline{H}_A H_B,\ Q_{B-L} = \overline{H}_B H_C,\ Q_{C-L} = \overline{H}_C H_A \quad (4)$$

$$Q_{A-H} = H_A \overline{H}_B,\ Q_{B-H} = H_B \overline{H}_C,\ Q_{C-H} = H_C \overline{H}_A \quad (5)$$

Figure 9 shows the expressions from the equations in graphical form.

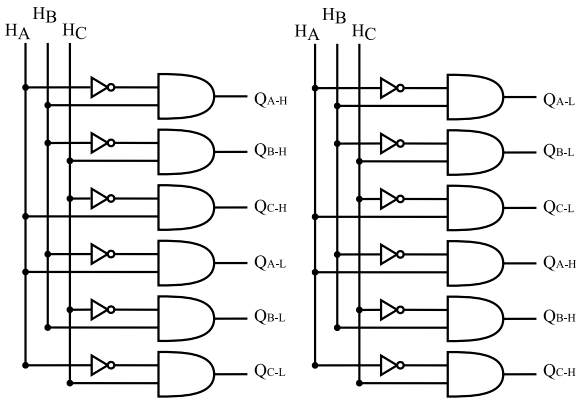

Figure 9: 120° Square-wave Commutation Logic (Left: Clockwise, Right: Counterclockwise).

Usually, a microcontroller is used to control a BLDC motor directly and this logic is implemented in software. For three-phase motors with Hall sensors six PWM output pins are required to control the H-bridge switches and three pins to sense the sensors. To reduce the performance requirements on the microcontroller (pin number, amount of instructions need to be processed within interrupt handler) a hardware commutation solution is proposed in form of a logical circuit based on discrete logic. One of the difficulties is to realize both rotational directions in a single circuit using minimal number of components for PCB space saving. Figure 10 shows a possible solution for bipolar switching (low and high side switches are modulated with the PWM synchronously). There are five input and six output signals. The inputs are the Hall sensor signals (H_A, H_B, H_C), the PWM signal S_{PWM} and the rotational direction D, whereby D only is connected to one of the microcontroller's GPIOs. The circuit consists of a demultiplexer stage, a XOR stage and a multiplexer stage. The PWM signal is guided through two 3-line to 8-line inverting demultiplexers using the three Hall sensor signals as selectors. In the second stage the signals are logically interconnected using six XOR gates. In the third stage the XOR outputs are guided through six 2-line multiplexers to control the rotational direction.

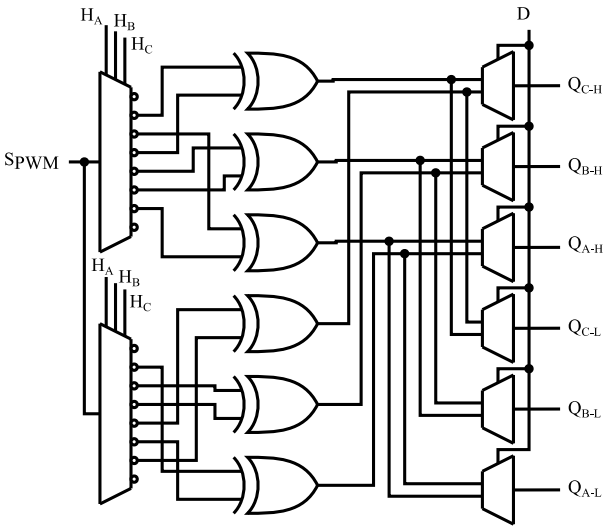

Figure 10: 120° Square-wave Commutation Logic Realized with Discrete Components.

The total number of ICs in the solution could be reduced to four ICs only, as multiple XOR gates or multiplexers are combined in dedicated single chip solutions. The footprint for the solution based on QFN packages measures 15 x 25 mm^2 (see Figure 12, one side PCB layout). The commutation circuit can be realized in Hi-Rel without re-design, because all semiconductors are available in both, commercial and Hi-Rel versions. Using the advanced high-speed CMOS logic (AHC) guarantees small propagation delays of some nanoseconds in the whole operational temperature range (see Figure 13).

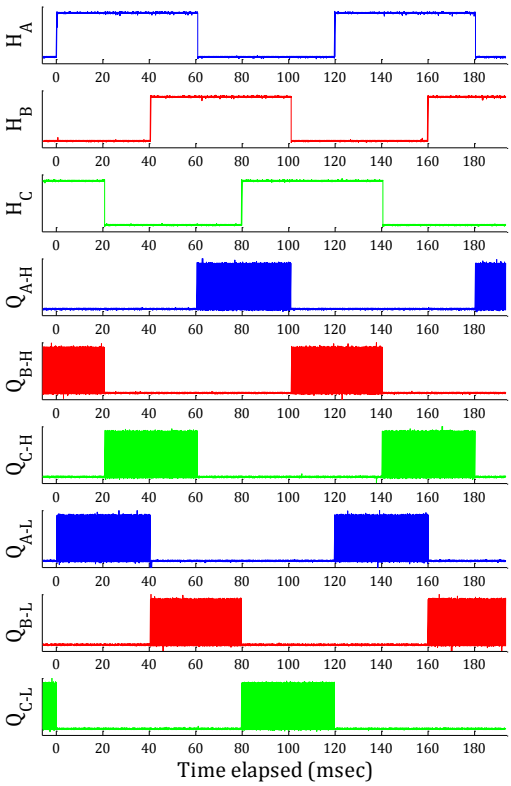

Figure 11: Measured Signals of the Commutation Circuit for Clockwise Rotation at 500 rpm.

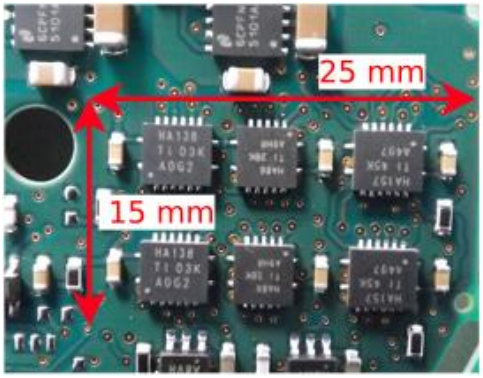

Figure 12: Footprint of Commutation Circuit.

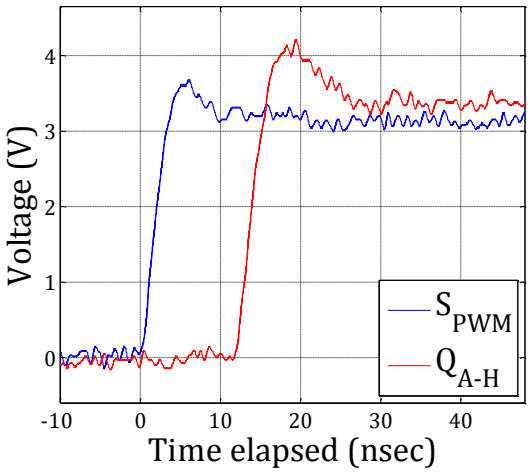

Figure 13: Propagation Delay through Commutation Circuit.

CONTROL

Figure 14 depicts a simplified diagram (Matlab) of the system that is used to design the control parameters of the wheel. The start point of the diagram is the current I through the coils of the motor. It comes from the switches of the H-bridge controlled by the commutation circuit and the PWM generator. The duty-cycle of the PWM signal and, consequently, the current I are controlled by the microcontroller unit (MCU). The current I is limited by a dynamic saturation value depending on actual rotational speed. With a known value for I the motor torque M that accelerates the flywheel can be calculated using the torque constant of the motor k_M. The friction torque may be taken into consideration by using the dynamic friction constant of the motor C_V. It depends on the rotational speed n. The gas friction (pressurized design) is not taken into account in this simplified model. The speed of rotation can be calculated from the torque M using the moment of inertia of the rotor J_{rot} (734 g cm^2) via integration of the angular acceleration. At none-zero rotational speeds a voltage is induced in the coils and can be calculated using the back-EMF constant of the motor k_E. This voltage (V_E) limits the current dynamically in dependence of the rotational speed. The difference between the supply voltage of the motor V_{mtr} and V_E is used to calculate the current limit at given rotational speed. For that purpose a reciprocal of the coil resistance R it used (4.36 Ohm).

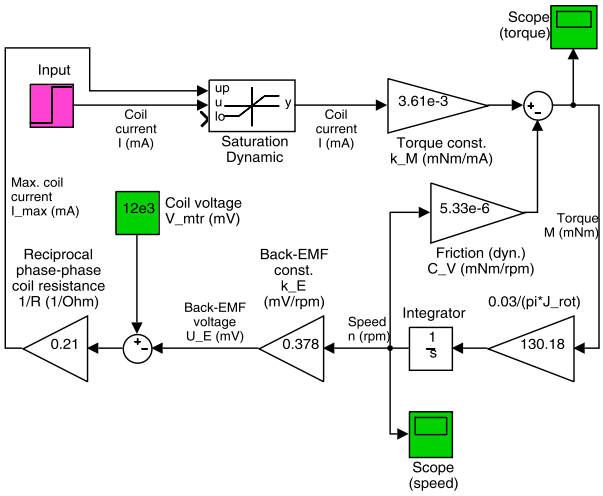

Figure 14: Simplified Block Diagram of the Motor.

Figure 15 depicts a simplified diagram of the circuits responsible for setting and measuring of the current. The six high-side and low-side MOSFETs of the H-bridge are simplified through two (currently active) only. The current controlled by the H-bridge flows through the coils of the motor represented by the resistance R. The current is amplified by a current monitor with an amplification factor of 20. The analog voltage representing the current is filtered in a low-pass filter built by C1…C5 and R1…R4. The purpose of the first stage of the low-pass filter (built of R1, R2, C1, C2 and C3) is to smooth the major spikes introduced by the PWM switching of the power MOSFETs and to protect the inputs of the current monitor. This stage has a cut-off frequency of approximately 350 Hz. The second stage of the low-pass filtering (built of R3, R4, C4 and C5) has a cut-off frequency of 16 Hz and used to stabilize the current control loop. The voltage proportional to the current is sampled by an analog-to-digital converter (ADC, 16 bit) with a reference voltage of 4.096 Volt. For the shunt resistance of 0.39 Ohm the maximal resolution for current measurement can be calculated using following equation:

$$I_{RES} = \frac{U_{REF}}{R_{shunt} K_{CurMon} ADC_{Count}} = \\ = \frac{4.096}{0.39 \cdot 20 \cdot 65535} = 8 \cdot 10^{-3} mA \quad (6)$$

The maximal value of the torque M_{MAX} results from the highest measurable current I_{MAX} using following equations:

$$I_{MAX} = ADC_{Count} I_{RES} = 524\,mA \quad (7)$$

$$M_{MAX} = k_M I_{MAX} = 3.61 \cdot 10^{-3} \frac{mNm}{A} \cdot 524\,mA = 1.9 mNm \quad (8)$$

All control loops are implemented in microcontroller in general form as PID (proportional-integral-derivative) controller. The proportional, integral and derivative terms (k_P, k_I, k_D) can be changed via command interface. The controller terms can be switched off by commanding a zero. For example, for the current control loop a simple I-controller is used (both k_P and k_D take zero values). The current loop is closed every 5 milliseconds. Figure 16 depicts the step response by commanding of a current of 50 mA.

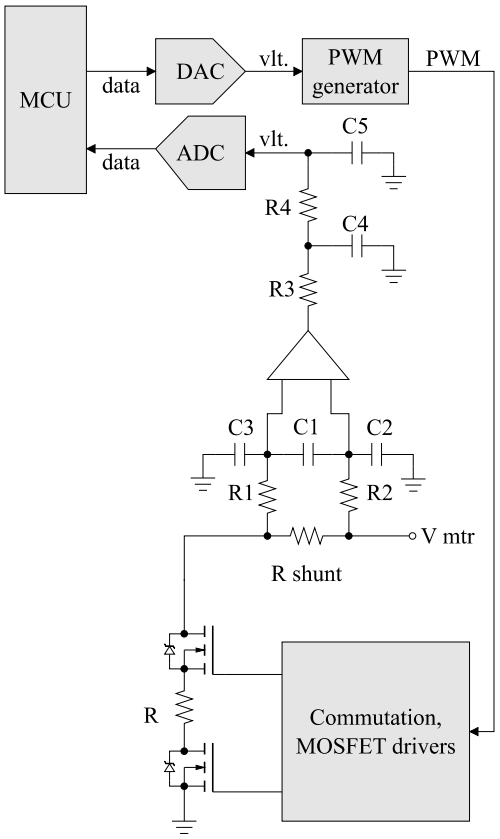

Figure 15: Simplified Block Diagram of the Current Set and Measure Circuits.

All further control loops except for the already described current control loop and the angle loop are implemented as cascades closed every 50 milliseconds. The inner loop (5 milliseconds) is the current control loop. This architecture is a compromise of a good stability, high accuracy and an acceptable speed.

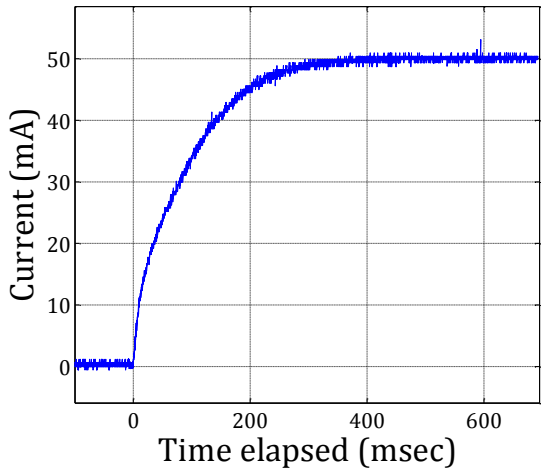

Figure 16: Step Response of Motor Current Loop.

To control the rotational speed of the motor a controller in PI-form is implemented. A step answer for a step of 500 to 1000 rpm is shown in Figure 17 (current is limited by the algorithm at the beginning). Despite of three Hall-effect sensors only to measure the rotational speed a good controller performance can be observed down to approximately 50 rpm with a constant close rate of 20 Hz (50 msec). With some controller designs control of very slow motor speeds below 50 rpm could be demonstrated on ground.

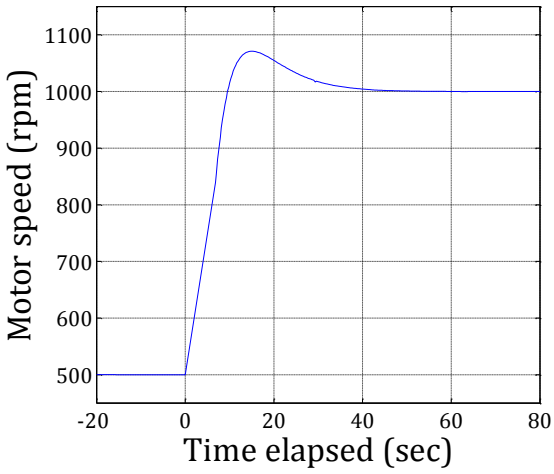

Figure 17: Step Response of Motor Speed Loop.

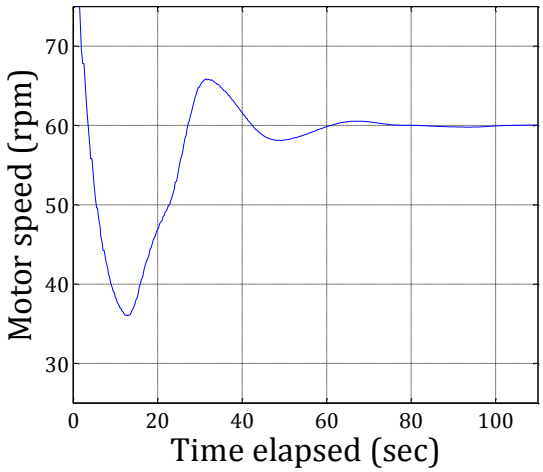

Figure 18: Motor Speed Loop at 60 rpm.

The torque control is the most challenging mode in a system without additional rotor position encoder. The torque mode is, in fact, a motor speed ramp mode ($\dot{n}$ in rev/min^2). The torque can be easily calculated from $\dot{n}$ using moment of inertia of the rotor J_{rot}. To get the rotational speed n and the first deviation of it $\dot{n}$ a time difference between adjacent edges of some rotor position sensor needs to be measured. The Hall-effect sensors provide six edges per revolution only (see Figure 11). At small rotation speeds it leads to a very large time the algorithm gets a new measurement compared to the loop time (50 msec). It is also a problem for the motor speed mode. For torque mode there is an additional difficulty due to the Hall sensor concept – the phase noise.

In general, the output of the Hall sensors is an analog voltage proportional to the magnetic field of the permanent magnet of the rotor. The built-in electronic components of the BLDC motor use some voltage comparators to construct rectangular signals from these voltages. During this conversion an additional noise is added to the noise of the Hall sensors. For a first approximation this noise does not depend on the rotational speed.

The time between the edges of the Hall sensors can be expressed as the sum of some positive average time $\Delta t'$ and a time-variant (but not rotational speed-variant) noise component Δt_N with a mean value centered around zero:

$$\Delta t = \Delta t' + \Delta t_N \qquad (9)$$

It is easy to see that on higher rotational speeds, if $\Delta t'$ decreases and the variance of Δt_N remains on a constant level, the relative noise component in Δt would increase. Consequently, it can be challenging to get a correct value for n and especially for $\dot{n}$ on higher speeds.

In practice, an averaging was used to calculate n and $\dot{n}$. To avoid a further error due to not exact angular positions of the Hall sensors the rising edge of one of the three Hall sensors is used as reference. For the torque loop a PI-controller is used. It performs well up to rotational speeds as high as 3000 rpm (see Figure 19) with a rapid decrease towards 6000 rpm.

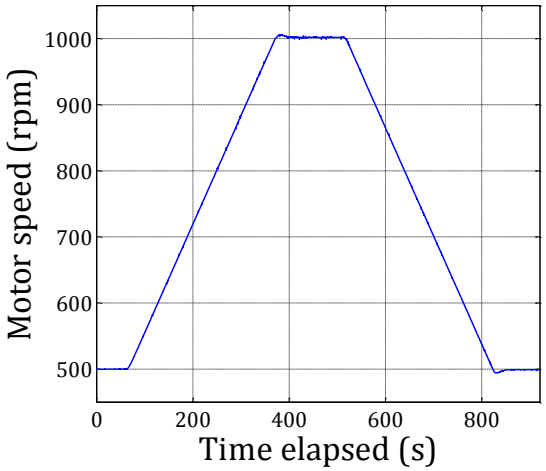

Figure 19: Torque Control with +100 rpm/min and -100 rpm/min.

The next loop is the satellite angular velocity mode. It is possible because of an integrated MEMS gyroscope. This mode allows an interactive attitude control, whereby the movements of the satellite can be easily controlled by the operator on ground using a joystick or similar devices [3]. Figure 20 depicts a system answer for ±1°/sec and ±0.5°/sec steps in one axis.

The satellite angle loop works similar with the exception that this loop is a cascade with two internal loops – the motor current control loop and the angular velocity control loop. At each new commanded (set) value the actual (working) value for the angle is cleared to zero. The angle setting is always relative. Figure 21 depicts a system answer for ±5° and ±10° steps.

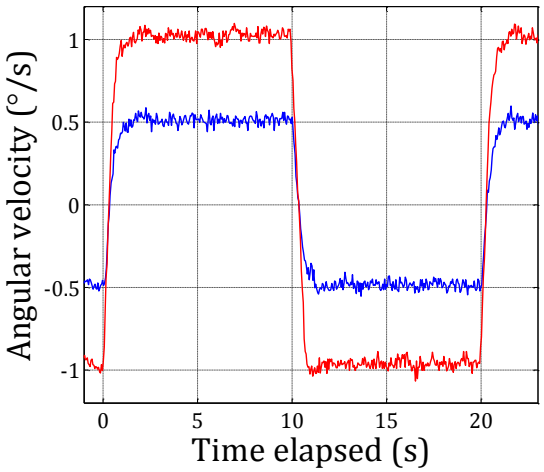

Figure 20: Satellite Angular Velocity Control with Reaction Wheel in Stand-alone Mode.

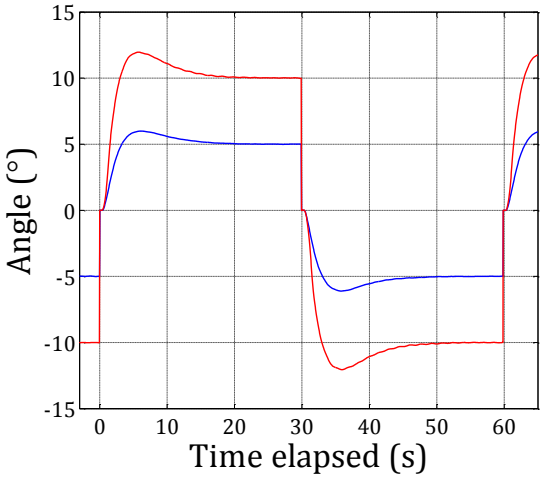

Figure 21: Satellite Angle Control with Reaction Wheel in Stand-alone Mode.

FLIGHT RESULTS

Before application, newly developed reaction wheel technology is comprehensively tested to ensure flawless functioning in orbit. However, the space environment cannot be completely reproduced on the ground and thus in-orbit demonstration (IOD) is of very high significance. The on-orbit verification results described here were gathered through 2018 and 2019 from the four nanosatellites of the S-Net mission.

All reaction wheels could withstand the mechanical loads during the launch without failures or losses in performance. The barometric pressure within the structure is still nominal (June 2019, S-Net is 15

months in orbit, TechnoSat is 2 years in orbit) confirming the sealing process and the assembly procedure.

Figure 22 depicts a typical measured change in pressure over a time of three full orbits. The changes are due to temperature differences (LEO with a high inclination). In a closed inner space of the wheel with a constant volume of gas included in it the relation between the pressure and the temperature can be expressed by the Law of Gay-Lussac. So the pressure can be easily predicted if the temperature is known. Following example shows a simple calculation of the lowest value pressure during eclipse P_{ECL} if the highest pressure during the Sun phase P_{SUN} as well as the both corresponding temperatures T_{SUN} and T_{ECL} are known.

$$P_{ECL} = P_{SUN} \frac{T_{ECL}}{T_{SUN}} = 866mbar \frac{274K}{284K} = 836mbar \quad (10)$$

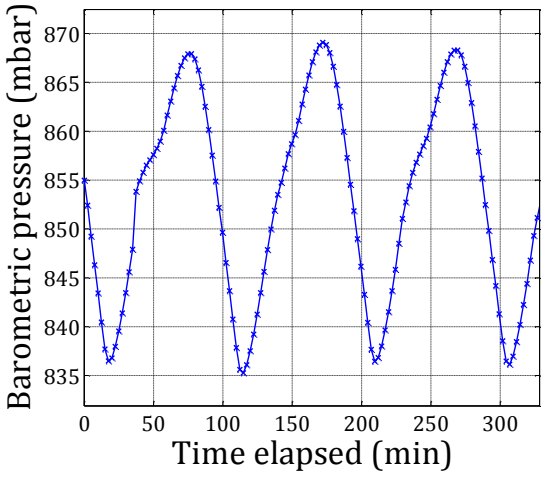

Figure 22: On-Orbit Measured Barometric Pressure.

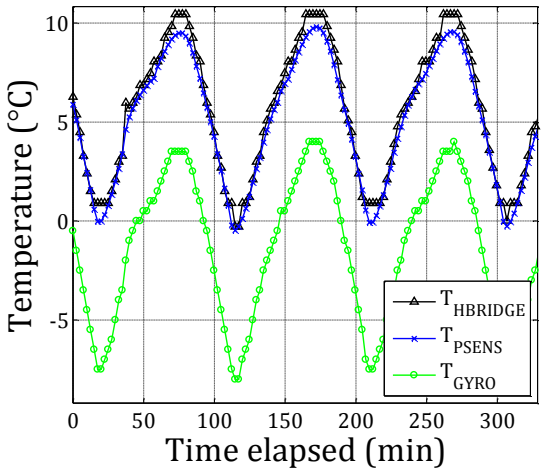

Figure 23: On-Orbit Measured Temperatures.

In S-Net satellites the wheels are controlled using the torque mode for detumbling, nadir-pointing and target-pointing. An example for detumbling is shown in Figure 24 and Figure 25.

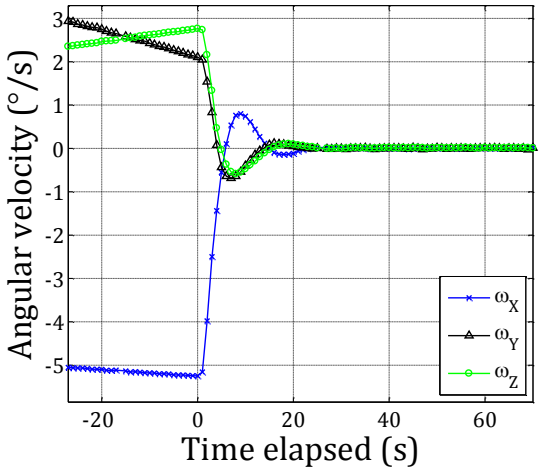

Figure 24: Satellite Angular Velocitiy for Detumbling Mode with Reaction Wheels (On-Orbit).

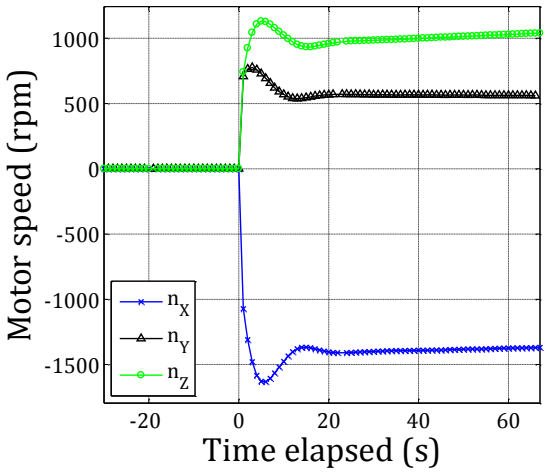

Figure 25: Motor Speed for Detumbling Mode with Reaction Wheels (On-Orbit).

CONCLUSIONS, FURTHER WORK AND ACKNOWLEDGEMENTS

The reaction wheels demonstrated a good performance and durability up to exceptional high rotation speeds of near 10000 rpm (nominal range: -6000…6000 rpm) over a period of more than one year in S-Net mission and over two years in TechnoSat mission. The motor suspension based on a novel principle is verified and worked as expected. The sealing procedure is confirmed; the inner space of all wheels remained hermetic after launch and during operation on-orbit. The reaction wheel is up-scalable with small modifications, e.g. in filter design and component selection for the H-bridge.

The performance of the wheels in torque mode on low speeds can be improved using additional rotor position encodes though it would lead to a higher energy consumption. The flywheel could get a slightly different shape (higher along the rotation axis) in order to achieve lower values of dynamic unbalance.

The project S-Net was implemented on behalf of the Federal Ministry of Education and Research (ger. Bundesministerium für Bildung und Forschung, BMBF) under grant number 50YB1225.

REFERENCES

1. Robert Schulte, "TUBSAT-N, A Global Communication Satellite System, based on Nanosatellites", Proceedings of the 4th International Symposium on Small Satellite Systems and Services, Antibes, France 1998.
2. Stefan Schulz, U. Renner. "DLR-TUBSAT: A Mircosatellite for Interaktive Earth Observation". Proceedings of the 5th International Symposium on Small Satellite Systems and Services, La Baule, France 2000.
3. Stephan Roemer, "Flight Experiences with DLR-TUBSAT," Proceedings of the IAA Symposium on Small Earth Observation Satellites, Berlin, 2000.
4. Frank Baumann, Hakan Kayal, Klaus Brieß, "BEESAT – A Fault-tolerant Picosatellite Approach", Proceedings of the 7th IAA Symposium on Small Satellites for Earth Observation, Berlin, 2009.